CHEMISTRY OF MATERIALS

Article

pubs.acs.org/cm

Feasibility of Using Li_2MoO_3 in Constructing Li-Rich High Energy Density Cathode Materials

Jun Ma,[†,⊥] Yong-Ning Zhou,[‡,⊥] Yurui Gao,[†] Xiqian Yu,[‡] Qingyu Kong,*[,§] Lin Gu,[∥] Zhaoxiang Wang,*[,†] Xiao-Qing Yang,*[,‡] and Liquan Chen[†]

[†]Key Laboratory for Renewable Energy, Chinese Academy of Sciences; Beijing Key Laboratory for New Energy Materials and Devices; Beijing National Laboratory for Condensed Matter Physics; Institute of Physics, Chinese Academy of Sciences, PO Box 603, Beijing 100190, China

[‡]Department of Chemistry, Brookhaven National Laboratory, Upton, New York 11973, United States

[§]X-ray Science Division, Argonne National Laboratory, 9700 South Cass Avenue, Argonne, Illinois 60439, United States

[∥]Laboratory for Advanced Materials & Electron Microscopy, Beijing National Laboratory for Condensed Matter Physics, Institute of Physics, Chinese Academy of Sciences, PO Box 603, Beijing 100190, China

Supporting Information

ABSTRACT: Layer-structured $xLi_2MnO_3\cdot(1-x)LiMO_2$ are promising cathode materials for high energy-density Li-ion batteries because they deliver high capacities due to the stabilizing effect of Li_2MnO_3. However, the inherent disadvantages of Li_2MnO_3 make these materials suffer from drawbacks such as fast energy-density decay, poor rate performance and safety hazard. In this paper, we propose to replace Li_2MnO_3 with Li_2MoO_3 for constructing novel Li-rich cathode materials and evaluate its feasibility. Comprehensive studies by X-ray diffraction, X-ray absorption spectroscopy, and spherical-aberration-corrected scanning transmission electron microscopy clarify its lithium extraction/insertion mechanism and shows that the Mo^{4+}/Mo^{6+} redox couple in Li_2MoO_3 can accomplish the task of charge compensation upon Li removal. Other properties of Li_2MoO_3 such as the nearly reversible Mo-ion migration to/from the Li vacancies, absence of oxygen evolution, and reversible phase transition during initial (de)lithiation indicate that Li_2MoO_3 meets the requirements to an ideal replacement of Li_2MnO_3 in constructing Li_2MoO_3-based Li-rich cathode materials with superior performances.

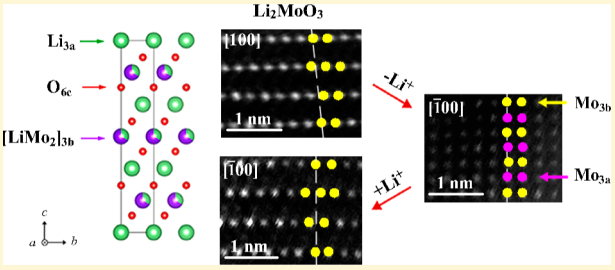

INTRODUCTION

Li-ion batteries (LIBs) have been powering most of the portable electronics for decades and are driving various types of electric vehicles nowadays. Safety, energy density, and cycle life are the essential criteria to evaluate if an LIB (or its pack) can be applied in these facilities. Mn-based Li-rich layer-structured oxide composites (or solid solutions) $xLi_2MnO_3\cdot(1-x)LiMO_2$ ($0 < x < 1.0$, M = Mn, Ni, Co, etc.) are promising cathode materials with reversible capacities above 280 mAh g^{-1} due to the stabilizing effect of the Li_2MnO_3 component on its structure.[1] However, the intrinsic properties of Li_2MnO_3, including the charge transfer from O^{2-} after oxygen release[2] or exchange of Li^+ by H^+, which is generated in the electrolyte[3] instead of the oxidation of Mn^{4+} ions, as well as the irreversible Mn^{4+}-ion migration into the lithium vacancies in the transition metal layer during the initial delithiation,[4] irreversible layer-to-spinel transition in subsequent Li^+ insertion,[5] and poor electrochemical kinetics,[6,7] make the composites suffer from drawbacks such as low initial Coulombic efficiency,[8] falling of discharge voltage and energy density,[4,9,10] and poor rate performance[11] during cycling as well as potential safety hazard caused by oxygen release[12,13] in the initial charge. Although surface modification,[14,15] atomic substitution,[16−18] and optimization of synthesis strategies[19,20] have been pursued to improve the performances of the composites, complete elimination of their drawbacks related to the Li_2MnO_3 component cannot be accomplished. Therefore, search for a replacement of Li_2MnO_3 that is compatible with $LiMO_2$ but is free of the disadvantages of Li_2MnO_3 is critical in designing novel Li-rich cathode materials $xLi_2M'O_3\cdot(1-x)LiMO_2$ ($0 < x < 1.0$, M' = Ti, Mn, Zr, Ru, Mo, Sn, Pt, Ir, etc.) with improved electrochemical performances.

Here, we propose to replace Li_2MnO_3 with Li_2MoO_3 with disordered $NaFeO_2$ structure ($R\bar{3}m$; a = 2.884 Å, c = 14.834 Å)[21−24] to construct novel Li-rich $xLi_2MoO_3\cdot(1-x)LiMO_2$ cathodes and evaluate its feasibility by X-ray diffraction (XRD), X-ray absorption spectroscopy (XAS) and spherical-aberration-corrected scanning transmission electron microscopy (STEM). This proposal was made on the basis of the following considerations and/or facts. (1) The Mo^{4+}/Mo^{6+} redox couple

Received: March 22, 2014
Revised: April 30, 2014
Published: May 1, 2014

in Li_2MoO_3 can exchange multiple electrons and supply a theoretical capacity up to 339 mAh g^{-1}. (2) Our first-principles calculations indicate that Mo doping delays the oxygen release (i.e., oxygen evolution occurs only when more Li ions are extracted) and lowers the potential of lithium extraction of Li_2MnO_3, beneficial for improving its structural stability and compatibility with the electrolyte.[25] (3) The similarity of lattice parameter of the hexagonal Li_2MoO_3 to that of $LiMO_2$ is beneficial for forming layer−layer solid solutions.[26−28] (4) Although Li_2MoO_3 was ruled out as an independent cathode due to the disproportionation and migration of its Mo ions in the first cycle,[21] that does not necessarily prevent it from becoming an ideal building block for constructing novel layer-structured cathode materials, $xLi_2MoO_3\cdot(1-x)LiMO_2$. Actually, $xLi_2MoO_3\cdot(1-x)LiFeO_2$ has been used as a cathode additive to improve the electrochemical performance of $LiCoO_2$ based cathode system.[29] (5) Black Li_2MoO_3 is expected to have a higher electronic conductivity than the red Li_2MnO_3, based on their colors (Figure S1). (6) Our recent studies indicate that Li_2MoO_3 is pretty stable in air, ensuring the air-stability of its related compounds.[30] Therefore, Li_2MoO_3 is considered as a possible replacement of conventional Li_2MnO_3 in building new layer-structured $xLi_2MoO_3\cdot(1-x)LiMO_2$ cathode materials. The features Li_2MoO_3 demonstrated in this article such as the reversible Mo-ion migration to/from the Li vacancies in the transition metal layer and the quasi-reversible electron transfer to/from the O^{2-} ions (without oxygen release) prove that Li_2MoO_3 can be an ideal replacement of Li_2MnO_3 in constructing novel Li-rich cathode materials $xLi_2MoO_3\cdot(1-x)LiMO_2$ with superior cycling stability, rate performance and safety. The basic findings in this work will also shed light on understanding and improving the voltage and capacity dropping of the conventional $xLi_2MnO_3\cdot(1-x)LiMO_2$ materials.

RESULTS AND DISCUSSION

Structure of As-Prepared Li_2MoO_3. The refined XRD pattern of the as-prepared Li_2MoO_3 powder matches well with the α-$NaFeO_2$ structure $R\bar{3}m$ with lattice constants a = 2.8675(9) Å and c = 14.8357(6) Å (Figure 1a and b and Supporting Information Table S1). The high intensity ratio (ca. 1.27) of (003)/(104) and clear splitting of the (018)/(110) diffraction peaks suggest the well-defined layered structure with very few antisite occupations concerning the Li^+ (3a site) and Mo^{4+} (3b sites) ions in the as-prepared Li_2MoO_3.[31−33] These are supported, in the atomic scale, with the investigation of STEM imaging (Figure 1c−f and Supporting Information Figure S2). These features ensure the good electrochemical performance of the material and the reliability of physical and electrochemical properties.

It is worthwhile to point out that the contrast of the high-angle annular-dark-field (HAADF) image exhibits a $Z^{1.7}$ dependence as compared with $Z^{1/3}$ for the annular-bright-field (ABF) image with respect to the atomic number Z.[34,35] The ABF image unambiguously displays the 3a-sited Li, 3b-sited Mo, and 6c-sited O-ion columns, while the HAADF image only displays the Mo-ion columns clearly. Due to the random distribution of the Li ions at the 3b sites, the 3b-sited Li-ion columns are superposed with the 3b-sited Mo-ion columns and could not be separately identified in Figure 1c and d. Figure 1e compares the line contrast profiles of the Li-, Mo- and O-ion columns along the $[42\bar{1}]$ direction projected on the [100] zone axis. However, in the as-prepared Li_2MoO_3, the Mo-ion

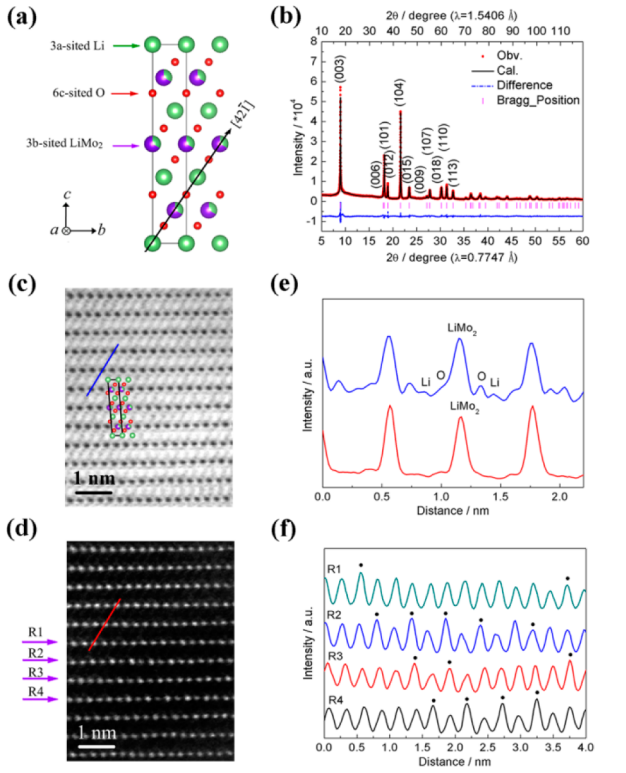

Figure 1. Structure of as-prepared Li_2MoO_3. (a) Schematic lattice of Li_2MoO_3. (b) The refined XRD pattern of Li_2MoO_3 (λ = 0.7747 Å) using GSAS program. (c) ABF STEM image of Li_2MoO_3 along the [100] zone axis with Mo ions in slipped $\alpha\beta\gamma$-stacking (O3 type). (d) The corresponding HAADF STEM image of part c. The bright dots represent Mo-ion column. (e) The corresponding line contrast profile of the Li, Mo, and O in parts c and d along the $[42\bar{1}]$ direction with the image contrast of dark dots in part c inverted and displayed as peaks. (f) The corresponding line contrast profiles of the Mo ions in part d along the marked rows. The marked black solid circle presents the much strong contrast of Mo-ion column.

columns show an $\alpha\beta\gamma$-stacking with an irregular shift along the [010] direction (slipped O3 type; Supporting Information Figure S3), due to the presence of disordered Mo_3O_{13} clusters in the Li−Mo layers (Supporting Information Figure S4). In addition, the presence of the short-range ordered distribution of the Mo_3O_{13} clusters is evidenced by the strong and weak contrast alternation in some areas in Figure 1d and f. The areas without such alternation are attributed to the disordered Mo_3O_{13} clusters (Supporting Information Figure S5).

Structural Transition and Mo-Ion Migration. Irreversible migration of the Mn ions into the transition metal layer to fill out the Li vacancies (a proposed layer-to-spinel transition) has been reported to be one of the causes for the capacity decay and discharge voltage dropping of the $xLi_2MnO_3\cdot(1-x)LiMO_2$ cathode materials. There are three charge plateaus but only one discharge slope in the first-cycle voltage profile of Li_2MoO_3 (Supporting Information Figure S6−S8). The slope corresponds to a reversible capacity of 210 mAh g^{-1} (when cycled between 2.0 and 4.5 V vs Li/Li^+) or ca. 190 mAh g^{-1} (when cycled between 2.0 and 4.8 V)—any of which is much higher than that of Li_2MnO_3.[36] The fact that the material charged to 4.5 V should have a higher reversible capacity than the one charged to 4.8 V is attributed to the destructive structural variation of Li_2MoO_3 when too many Li ions are extracted.

dx.doi.org/10.1021/cm501025r | Chem. Mater. 2014, 26, 3256−3262

In order to investigate the structural changes of Li_2MoO_3 during electrochemical (de)lithiation between 2.0 and 4.8 V, in situ XRD characterization was performed (Figure 2a and

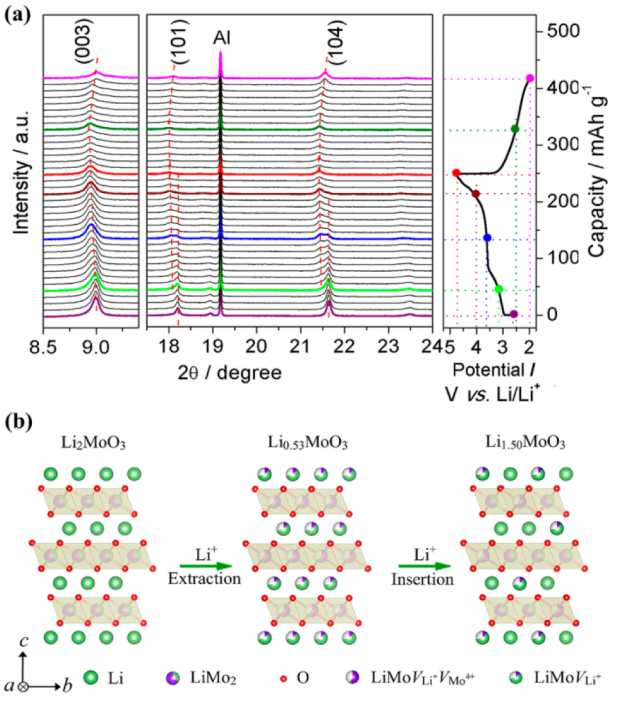

Figure 2. Structural evolution of Li_2MoO_3 during the initial delithiation and lithiation. (a) *In situ* XRD patterns of $Li_{2-x}MoO_3$ ($0 \le x \le 2$) electrodes while a Li_2MoO_3/Li cell is charged and discharged at a current density of 10 mA g^{-1} between 2.0 and 4.8 V. (b) Schematic structures of $Li_{2-x}MoO_3$ ($0 \le x \le 2$) (V representing atomic vacancy) during the initial charge and discharge process.

Supporting Information Figure S9). Before the cell is charged to ca. 3.1 V, a solid-solution reaction occurs with negligible variation of cell parameters ($Li_2MoO_3 \rightarrow Li_{1.75}MoO_3 + 0.25Li^+$).

As the cell is further charged to ca. 3.6 V, the (003) diffraction peak shifts to lower angles and gradually becomes broader. Meanwhile, the intensities of the other peaks indexed to Li_2MoO_3 decrease while those of new peaks indexed to $Li_{0.91}MoO_3$ phase ($R\bar{3}m$; a = 2.906 Å, c = 14.904 Å; Supporting Information Figure S10) at ca. 18.0° and 21.4° become increasingly stronger.[21] The phase transition from Li_2MoO_3 to $Li_{0.91}MoO_3$ is finished at ca. 4.0 V ($Li_{1.75}MoO_3 \rightarrow Li_{0.75}MoO_3 + 1.00\ Li^+$), suggesting that Li-ion vacancies appear at both the 3a and 3b sites and that some 3b-sited Mo ions have migrated to fill the 3a sites (Figure 2b). Above 4.0 V, the position shifting of the $Li_{0.91}MoO_3$ peaks stops though more Li ions are extracted ($Li_{0.75}MoO_3 \rightarrow Li_{0.53}MoO_3 + 0.22Li^+$). Instead, they become broader and their intensities decrease gradually. This implies the start of another solid-solution reaction with degraded crystallinity and/or reduced crystallite size, consistent with the destruction of the lattice fringe in the high resolution transmission electron microscopy (HRTEM) images (Supporting Information Figure S11).

In the subsequent Li-ion insertion process, these diffraction peaks keep unchanged at first ($Li_{0.53}MoO_3 + 0.44Li^+ \rightarrow Li_{0.97}MoO_3$) and then continuously shift to higher diffraction angles very close to that of Li_2MoO_3 ($Li_{0.97}MoO_3 + 0.53Li^+ \rightarrow Li_{1.50}MoO_3$). Meanwhile, the intensities of the peaks increase with Li-ion insertion. Interestingly, the insertion of Li ions to $Li_{0.53}MoO_3$ and $Li_{0.97}MoO_3$ seems to be a solid-solution reaction, different from that in the charge process. These indicate that the structure of Li_2MoO_3 can mostly be restored though the recovery is not along a reverse path of Li-ion extraction.

STEM HAADF images of Li_2MoO_3 at different states in the first charge and discharge processes were recorded to check the Mo-ion migration and the resultant structural transition during Li-ion insertion/extraction at the atomic scale (Figure 3 and

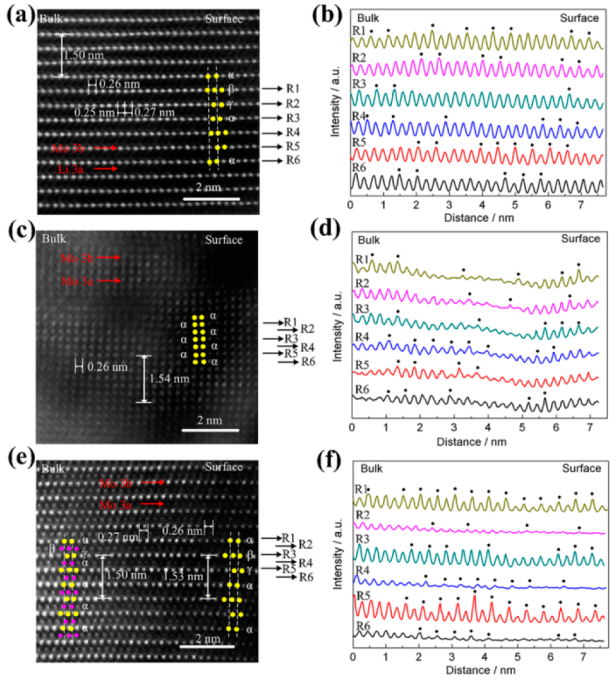

Figure 3. Detection of Mo-ion migration in atomic scale. (a) HAADF image of the as-prepared Li_2MoO_3 along the [100] zone axis. (c and e) HAADF images of the charged and discharged Li_2MoO_3 along the [$\bar{1}$00] zone axis, respectively. The Mo ions at 3a and 3b sites in the HAADF images are presented with pink and yellow solid circles, respectively. (b , d , and f) Corresponding line contrast profiles of Mo ions along the marked rows in the HAADF images. The much strong contrast of Mo ions is marked with black solid circle in the line contrast profiles.

Supporting Information Figure S12−S15). After Li-ion extraction, the Mo ions migrate from 3b to 3a sites, implying the disaggregation of the Mo_3O_{13} clusters. As a result, the atoms in the 3b and 3a sites have similar contrasts. An *ααα*-stack (O1 type; Supporting Information Figure S3) $Li_{2-x}MoO_3$ with many faults was obtained, including defects, distortion, and edge dislocation, induced by the stress during Li-ion extraction and Mo-ion migration. When the Li ions are inserted back to the charged Li_2MoO_3, the 3a-sited Mo ions on the surface partially disappear, but those in the bulk remain there. In both areas, the Mo ions show an *αβγ*-stack model (O3 type; Supporting Information Figure S3).

Phase transformation from faulted O1 type to O3 type seems to be the way that requires the lowest energy to bear the stress induced by the Li-ion insertion. The Mo−Mo distances parallel and vertical to the *c* axis are similar to those of the as-prepared sample during Li-ion extraction and insertion. Obviously, the alternatively strong and weak contrasts reappear in the 3b sites, suggesting the reconstruction of some ordered Mo_3O_{13} clusters.

dx.doi.org/10.1021/cm501025r | *Chem. Mater.* 2014, 26, 3256−3262

The difference between surface and bulk might be originated from the inhomogeneous insertion of the Li ions. Therefore, the partially reversible migration of the Mo ions and the partial recovery of the Mo_3O_{13} clusters are responsible for the partially reversible phase transition, consistent with the above in situ XRD results. These features would have significant impact on the structural and cycling stability of the to-be-prepared $xLi_2MoO_3\cdot(1-x)LiMO_2$ composites.

Extra Electron Donor and Charge Compensation. Oxygen release occurs in the first (few) cycle(s) of $xLi_2MnO_3\cdot(1-x)LiMO_2$ because the Mn^{4+} ions in Li_2MnO_3 cannot be further oxidized. O^{2-} ions are the single electron donor there. Replacing Mn^{4+} with Mo^{4+} is expected to provide another electron donor to, partially at least, release the charge compensation task of oxygen. Ex situ XAS at the Mo K-edge was performed in order to investigate the changes of the local structure and oxidation states of Mo in Li_2MoO_3 during charge and discharge. Figure 4a shows the X-ray absorption near edge spectra (XANES) of Mo K-edge at various states. The absorption edges shift to higher energy during charge. Using the reference spectra of MoO_2 and MoO_3 (Supporting Information Figure S16), the valence state of Mo is estimated to be changed from +4 to around +6 during Li-ion extraction. In addition, the intensity of the pre-edges increases after charge, due to the distortion of the MoO_6 octahedron resulting from the increasing O_{2p}–Mo_{4d} hybridization.[37−40] These imply that the MoO_6 octahedrons in the Mo_3O_{13} clusters and other parts of the as-prepared Li_2MoO_3 become more and more distorted with increasing Li removal.

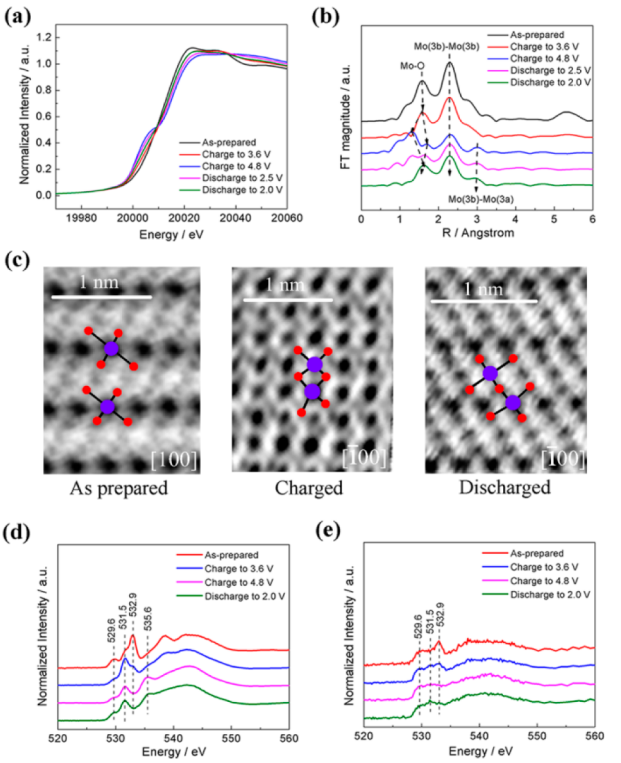

Figure 4. Charge compensation of Li_2MoO_3 during the initial delithiation and lithiation. (a) XANES spectra of Mo K-edge of Li_2MoO_3 at different delithiation and lithiation states. (b) Fourier-transformed Mo K-edge EXAFS spectra of Li_2MoO_3 corresponding to part a. (c) ABF imaging of Li_2MoO_3 at different delithiation and lithiation states showing the variation of the Mo–O distances, indicating the distortion of the MoO_6 octahedra during Li^+ extraction and insertion. (d) PEY mode and (e) FY mode of O K-edge soft XAS spectra of Li_2MoO_3 at different delithiation and lithiation states.

In the discharge process, however, the absorption edges shift back to lower energy but do not return to their original positions, suggesting that the Mo ions are reduced during Li-ion insertion, but their average valence state is still higher than Mo^{4+} even after full discharge. The reversible oxidation of the Mo^{4+} ions is consistent with the reversible reduction of the O^{2-} ions at the full discharge state as will be seen in the following discussion. Meanwhile, the intensity of the pre-edges is reduced but not completely recovered to that of the as-prepared Li_2MoO_3. This means that the local coordination environment around the Mo ions in the discharged sample is somewhere between that of the as-prepared and the partially charged Li_2MoO_3. This is further demonstrated with the Fourier transformed extended X-ray absorption fine structure (FT-EXAFS) spectra in Figure 4b and the ABF images in Figure 4c.

Two dominant peaks can be observed in the Mo K-edge FT-EXAFS spectrum of the as-prepared Li_2MoO_3 (Figure 4b). The peak at $R \sim 1.6$ Å belongs to the Mo–O bond in the nearest MoO_6 octahedra while the peak at $R \sim 2.3$ Å is attributed to the Mo–Mo bond in the a–b plane, consistent with the ABF imaging of the as-prepared Li_2MoO_3 that displays the projection of the MoO_6 octahedra and the Mo-ion arrangement along the [100] zone axis (Figure 4c). It should be noted that as the FT-EXAFS spectrum was not phase corrected, the actual lengths of the bonds are approximately 0.3–0.5 Å longer than those shown here.

The length of the Mo–O bond increases slightly but that of the Mo–Mo bond does not change at all when the material is charged to 3.6 V. When it is charged to 4.8 V, the Mo–O peak splits into two at around 1.3 and 1.7 Å, respectively, indicating that the MoO_6 octahedra are severely distorted and Mo–O bonds with different lengths are formed. The intensity of the Mo(3b)–Mo(3b) peaks decreases gradually, indicating the reduction of the number of the Mo ions at the 3b sites. In addition, a new peak appears at ~3.0 Å; it is attributed to the Mo(3b)–Mo(3a) bonding between the interlayers. These results confirm the Mo-ion migration from 3b to 3a sites during charge. These are further demonstrated clearly with the distorted projection of the MoO_6 octahedra as well as the contrast variation at both 3a and 3b sites in the ABF imaging of the charged Li_2MoO_3 (Figure 4c).

After discharged to 2.5 V, the two Mo–O peaks of the charged sample move toward each other. Meanwhile, the intensity of the Mo(3b)-Mo(3b) peak increases, implying that the severely distorted MoO_6 octahedra are changed back to their original states (Figure 4c). However, the changes of the Mo(3b)–Mo(3a) peak are not obvious, indicating that the Mo ions at the 3a sites do not move back to the 3b sites at this discharge state. After discharged to 2.0 V, the two Mo–O peaks of the material are merged into one and the intensity of the Mo(3b)–Mo(3b) peak increases back to its original value, suggesting the recovery of the regular MoO_6 octahedra and the reversible Mo-ion migration (Figure 4c). On the other hand, the Mo(3b)–Mo(3a) peak is still present but its intensity decreases slightly. All these suggest that the MoO_6 octahedra in the Li–Mo layer can be recovered but the Mo-ion migration between the 3b and 3a sites is only partially reversible. This is partially responsible for the irreversible capacity loss in the first cycle. These results are in good agreement with the in situ XRD and STEM results.

dx.doi.org/10.1021/cm501025r | Chem. Mater. 2014, 26, 3256−3262

The oxygen species play an important role in the safety and structural stability of the Li-rich layered materials.[2,12,13] Irreversible oxygen evolution in the first (few) cycle(s) results in safety hazard and structural degradation in Li_2MnO_3-based Li-rich cathode materials $xLi_2MnO_3\cdot(1-x)LiMO_2$. Recently, Tarascon et al.[41] reported that the Ru^{4+}/Ru^{5+} and O^{2-}/O^{-} redox couples instead of O_2 loss supplied the charge compensation during the (de)lithiation of $Li_2Ru_{1-x}Sn_xO_3$, which exhibited high reversible capacity and good cycling performance. With the assistance of partially reversible oxidation/reduction of the Mo^{4+}/Mo^{6+} redox couples in charge compensation in Li_2MoO_3 as shown above, we expect that the oxygen release in Li_2MnO_3 and $xLi_2MnO_3\cdot(1-x)LiMO_2$ can also be avoided or significantly suppressed. In order to find out if this is true in Li_2MoO_3, O K-edge soft XAS spectroscopy was used to determine the changes of the electronic structure of the oxygen. Figure 4d and e shows the O K-edge XAS spectra in the partial electron yield (PEY) and fluorescent yield (FY) modes, respectively. During charge, the hybridization of the O_{2p} and Mo_{4d} orbitals increases with increasing oxidation of Mo^{4+}, based on the decreased relative intensity of peaks at 532.9 and 529.6 eV and the increased intensity of the 531.5 eV peak.[26,42,43] A new peak appears at 535.6 eV in the surface-sensitive PEY spectrum as the material is charged to 4.8 V. This peak can be assigned to the $O^{(2-\sigma)-}$ $(0 < \sigma \leq 2)$ ions because higher energy is required to excite the O_{1s} electron in an oxidized O ion.[44] This implies that oxygen indeed participates in the charge compensation in Li_2MoO_3 during charge.

In the lithiation process, the intensity of the 535.6 eV peak decreases slightly, indicating that the charge compensation from oxygen is partially reversible. In contrast, the XAS spectra in the FY mode, which mainly give information about the bulk, show no obvious changes at 535.6 eV. This suggests that the charge compensation from the oxygen in Li_2MoO_3 mainly occurs on the surface of the particle. Hence, although charge compensation from the surface O^{2-} ions still occurs in deeply delithiated ($Mo^{4+} \rightarrow Mo^{6+}$) Li_2MoO_3, such compensation is at least partially reversible and is basically a kinetic rather than a thermodynamic effect in Li_2MoO_3. As a result, oxygen release can be suppressed to a great deal in a $xLi_2MoO_3\cdot(1-x)LiMO_2$ composite even when it is charged to 4.8 V. This will definitely enhance the safety and structural stability of Li_2MoO_3 and its related compounds or composites.

(De)lithiation Mechanism. Based on the above comprehensive XRD, STEM, and XAS studies of Li_2MoO_3 at various charge/discharge states, a possible phase transition diagram of $Li_{2-x}MoO_3$ $(0 \leq x \leq 1.47)$ can be drawn (Figure 5). At the beginning of charging $(0 \leq x \leq 0.25)$, a solid-solution reaction occurs due to the oxidation of the Mo ions and the slight distortion of the MoO_6 octahedra but the slipped O3–Li_2MoO_3 structure keeps unchanged (Region I). Three Mo ions in the Mo_3O_{13} cluster contribute to the charge compensation. As a result, the Mo–Mo bonds keep unchanged and no Mo-ion migration to the Li layer takes place at this stage. As more Li ions are extracted, the increased number of the Li vacancies and the oxidization of the Mo^{4+} ions enhance the Mo–O interactions gradually, resulting in the distortion of the MoO_6 octahedra. Consequently, some of the Mo–Mo bonds are broken and the Mo ions start migrating toward the Li vacancies (3a sites), leading to a Li_2MoO_3–$Li_{0.91}MoO_3$ two-phase reaction. The slipped O3-type stacking becomes distorted O1-type stacking (Region II) $(0.25 \leq x \leq 1.25)$. The complicated slope (Region III) is attributed to the solid-solution reaction of $Li_{2-x}MoO_3$ $(1.25 \leq x \leq 1.47)$ with increasing Li vacancies, the MoO_6 octahedron distortion and Mo-ion interlayer migration. In the discharge process (Regions IV and V), solid-solution reaction of $Li_{2-x}MoO_3$ occurs successively with decreasing MoO_6 octahedron distortion first $(1.03 \leq x \leq 1.47)$ and then migration of Mo ions back to the 3b sites $(0.50 \leq x \leq 1.03)$. As a result, distorted O1-type stacking of Mo ions transforms to Li-insufficient O3 type $Li_{2-x}MoO_3$. Some ordered Mo_3O_{13} clusters are also recovered in this process.

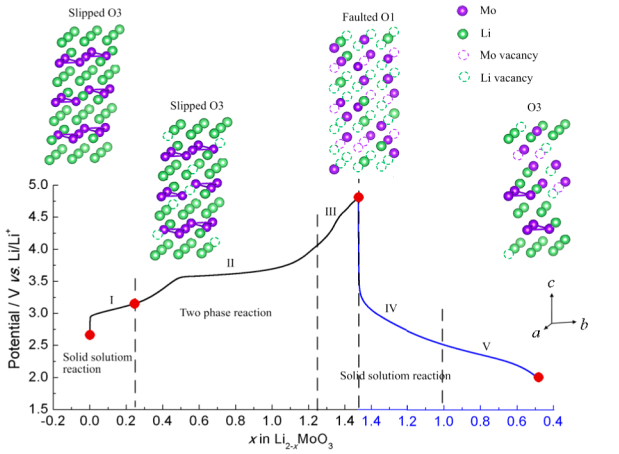

Figure 5. Structural transition of Li_2MoO_3 in the initial electrochemical (de)lithiation process. The lattice structure variation demonstrates that solid-solution reaction and two-phase reaction occur in consequence.

Although further experimental and theoretical studies are required to find out more details of the phase transitions during the initial and the subsequent cycles, such as the paths of the Li-ion diffusion and the Mo-ion migration, and the phase boundaries developed during (de)lithiation, the results in this paper clearly demonstrated that the phase transition in this material is, to a great deal, reversible upon the initial lithium insertion and extraction, thanks to the charge compensation effect of both Mo^{4+} and O^{2-} ions. This is distinctive from the complete structural destruction that occurs in Li_2MnO_3. Such phase transition features actually ensure the better structural and cycling reversibility of Li_2MoO_3 and, very possibly, for those of the Li_2MoO_3-related Li-rich layer-structured cathode materials.

It is the irreversible oxygen release and the transition metal migration in highly delithiated Li_2MnO_3 that lead to its irreversible structural transition and capacity loss. Different from that, introduction of the Mo^{4+}/Mo^{6+} redox couple in Li_2MoO_3 helps its charge compensation upon Li removal. Such joint charge compensation of the Mo^{4+} and O^{2-} ions lowers the degree of oxidation of O^{2-} and avoids the oxygen evolution. As a result of these, the oxidation of O^{2-} to $O^{(2-\sigma)-}$ is nearly reversible up to the extraction of around 1.5 Li per formula unit of Li_2MoO_3. The kinetic instead of thermodynamic requirements means that the reversibility of the $O^{2-}/O^{(2-\sigma)-}$ redox reaction can be improved even without modifying the structure of Li_2MoO_3. This provides more space for further improvement of the electrochemical performances of Li_2MoO_3 and its related composite cathode materials. In addition, considering the fact that the material charged to 4.5 V should have a reversible capacity than that charged to 4.8 V (Supporting Information Figure S7), it makes sense to believe that, in reality, Li_2MoO_3

dx.doi.org/10.1021/cm501025r | Chem. Mater. 2014, 26, 3256–3262

and Li_2MoO_3-based cathode materials do not need to be charged to such high (4.8 V) potentials. In that case, the reversibility of the Mo-ion migration and O^{2-}-ion oxidation, structural stability and the compatibility with electrolyte should be even better than shown here.

CONCLUSION

In summary, comprehensive in situ XRD and ex situ STEM and XAS studies clarify the electrochemical (de)lithiation mechanism of Li_2MoO_3 and prove the feasibility of replacing Li_2MnO_3 with its iso-structured Li_2MoO_3 to construct novel Li-rich cathode materials. The as-prepared Li_2MoO_3 shows a slipped O3-type stacking of the Mo ions with short-range ordered but long-range disordered Mo_3O_{13} clusters. During the initial delithiation, solid-solution reaction and then two-phase reaction take place in series and the Mo^{4+} ions are oxidized to Mo^{6+} ions. As the material is discharged, its structure is recovered to a Li-insufficient O3 type $Li_{2-x}MoO_3$ (x = 0.50) due to the incomplete reduction of Mo^{6+} ions, the partially reversible Mo_3O_{13} cluster and Mo-ion migration at the end of lithiation. Different from the irreversible oxygen release in deeply delithiated Li_2MnO_3, the oxidation of O^{2-} to $O^{(2-\sigma)-}$ is nearly reversible and is a dynamic rather than thermodynamic effect in Li_2MoO_3. Features such as reversible Mo-ion migration and O^{2-} oxidation upon lithium removal, facile charge compensation due to presence of the Mo^{4+}/Mo^{6+} redox couple have significant impacts on the structural stability and reversibility of Li_2MoO_3. Both the reversible structural transition (based on the reversible migration of the Mo ions) and the reversible charge transfer (with Mo^{4+} as another electron donor) demonstrate the feasibility of replacing Li_2MnO_3 with Li_2MoO_3 for constructing novel Li_2MoO_3-based Li-rich cathode materials with stronger structural stability and higher cycling reversibility. In addition, the findings on the contribution of covalent bond between transition metal ions bring new insight into the fundamental understandings of electrochemical (de)lithiation mechanism of Li-rich layer-structured oxides.

ASSOCIATED CONTENT

Supporting Information

Experimental section, refined structural parameters, SEM images of the as-prepared Li_2MoO_3, its electrochemical performance, the original STEM images and the corresponding charge/discharge potential profiles of Li_2MoO_3 at various (de)lithiated states, HRTEM images of Li_2MoO_3, schematic diagrams of Li_2MoO_3 structure, Mo K-edge XANES spectra of the reference compounds MoO_2 and MoO_3. This material is available free of charge via the Internet at http://pubs.acs.org/.

AUTHOR INFORMATION

Corresponding Authors

*Email: zxwang@iphy.ac.cn.
*Email: xyang@bn-l.gov.
*Email: qkong@aps.anl.gov.

Author Contributions

$^{\perp}$J.M. and Y.-N.Z. contributed equally to this work.

Notes

The authors declare no competing financial interest.

ACKNOWLEDGMENTS

This work was financially supported by the National Natural Science Foundation of China (NSFC No. 51372268) and the National 973 Program of China (2009CB220100). The work at Brookhaven National Laboratory was supported by the U.S. Department of Energy, the Assistant Secretary for Energy Efficiency and Renewable Energy, Office of Vehicle Technologies under Contract No. DEAC02-98CH10886. The authors acknowledge technical supports by the beamline scientists at X14A of NSLS and beamline scientists at 12BM of Advanced Photon Sources at Argonne National Laboratory.

REFERENCES

(1) Thackeray, M. M.; Kang, S.-H.; Johnson, C. S.; Vaughey, J. T.; Benedek, R.; Hackney, S. A. *J. Mater. Chem.* **2007**, *17*, 3112−3125.
(2) Lu, Z. H.; Dahn, J. R. *J. Electrochem. Soc.* **2002**, *149*, A815−A822.
(3) Robertson, A. D.; Bruce, P. G. *Chem. Commun.* **2002**, 2790−2791.
(4) Croy, J. R.; Kim, D.; Balasubramanian, M.; Gallagher, K.; Kang, S.-H.; Thackeray, M. M. *J. Electrochem. Soc.* **2012**, *159*, A781−A790.
(5) Yu, D. Y. W.; Yanagida, K.; Kato, Y.; Nakamura, H. *J. Electrochem. Soc.* **2009**, *156*, A417−A424.
(6) Bommel, A.; Dahn, J. R. *Electrochem. Solid-State Lett.* **2010**, *13*, A62−A64.
(7) Yu, H. J.; Wang, Y. R.; Asakura, D.; Hosono, E.; Zhang, T.; Zhou, H. S. *RSC Adv.* **2012**, *2*, 8797−8807.
(8) Bommel, A.; Krause, L. J.; Dahn, J. R. J. *Electrochem. Soc.* **2011**, *158*, A731−A735.
(9) Song, B. H.; Liu, Z. W.; Lai, M. O.; Lu, L. *Phys. Chem. Chem. Phys.* **2012**, *14*, 12875−12883.
(10) Yu, S. Y.; Yoon, T.; Mun, J.; Park, S.; Kang, Y.-S.; Park, J.-H.; Oh, S. M.; Sung, Y.-E. *J. Mater. Chem. A* **2013**, *1*, 2833−2839.
(11) Kang, S.-H.; Thackeray, M. M. *Electrochem. Commun.* **2009**, *11*, 748−751.
(12) Armstrong, A. R.; Holzapfel, M.; Novak, P.; Johnson, C. S.; Kang, S.-H.; Thackeray, M. M.; Bruce, P. G. *J. Am. Chem. Soc.* **2006**, *128*, 8694−8698.
(13) Xiao, R. J.; Li, H.; Chen, L. Q. *Chem. Mater.* **2012**, *24*, 4242−4251.
(14) Kang, S.-H.; Johnson, C. S.; Vaughey, J. T.; Amine, K.; Thackeray, M. M. *J. Electrochem. Soc.* **2006**, *153*, A1186−A1192.
(15) Wu, C. R.; Fang, X. P.; Guo, X. W.; Mao, Y.; Ma, J.; Zhao, C. C.; Wang, Z. X.; Chen, L. Q. *J. Power Sources* **2013**, *231*, 44−49.
(16) Mori, D.; Sakaebe, H.; Shikano, M.; Kojitani, H.; Tatsumi, K.; Inaguma, Y. *J. Power Sources* **2011**, *196*, 6934−6938.
(17) Deng, Z. Q.; Manthiram, A. *J. Phys. Chem. C* **2011**, *115*, 7097−7103.
(18) Park, J.-H.; Lim, J.; Yoon, J.; Park, K.-S.; Gim, J.; Song, J.; Park, H.; Im, D.; Park, M.; Ahn, D.; Paik, Y.; Kim, J. *Dalton Trans.* **2012**, *41*, 3053−3059.
(19) Liu, J. L.; Chen, L.; Hou, M. Y.; Wang, F.; Che, R. C.; Xia, Y. Y. *J. Mater. Chem.* **2012**, *22*, 25380−25387.
(20) Koga, H.; Croguennec, L.; Mannessiez, P.; Menetrier, M.; Weill, F.; Bourgeois, L.; Duttine, M.; Suard, E.; Delmas, C. *J. Phys. Chem. C* **2012**, *116*, 13497−13506.
(21) James, A. C. W. P.; Goodenough, J. B. *J. Solid State Chem.* **1988**, *76*, 87−96.
(22) Hibble, S. J.; Fawcett, I. D. *Inorg. Chem.* **1995**, *34*, 500−508.
(23) Hibble, S. J.; Fawcett, I. D.; Hannon, A. C. *Acta Crystallogr.* **1997**, *B53*, 604−612.
(24) Hibble, S. J.; Hannon, A. C.; Fawcett, I. D. *J. Phys.: Condens. Matter* **1999**, *11*, 9203−9219.
(25) Gao, Y. R.; Ma, J.; Wang, X. F.; Lu, X.; Bai, Y.; Wang, Z. X.; Chen, L. Q. *J. Mater. Chem. A* **2014**, *2*, 4811−4818.
(26) Ohzuku, T.; Ueda, A. *J. Electrochem. Soc.* **1994**, *141*, 2972−2977.
(27) Ueda, A.; Ohzuku, T. *J. Electrochem. Soc.* **1994**, *141*, 2010−2014.

(28) Cushing, B. L.; Goodenough, J. B. *Solid State Sci.* **2002**, *4*, 1487−1493.
(29) Park, K.-S.; Im, D.; Benayad, A.; Dylla, A.; Stevenson, K. J.; Goodenough, J. B. *Chem. Mater.* **2012**, *24*, 2673−2683.
(30) Ma, J.; Gao, Y. R.; Wang, Z. X.; Chen, L. Q. *J. Power Sources* **2014**, *258*, 314−320.
(31) Wulff, H.; Mohan Rao, M.; Scholz, F. *Chem. Mater.* **2003**, *15*, 988−993.
(32) Tran, N.; Croguennec, L.; Jordy, C.; Biensan, Ph.; Delmas, C. *Solid State Ionics* **2005**, *176*, 1539−1547.
(33) Lu, X.; Sun, Y.; Jian, Z. L.; He, X. Q.; Gu, L.; Hu, Y.-S.; Li, H.; Wang, Z. X.; Chen, W.; Duan, X. F.; Chen, L. Q.; Maier, J.; Tsukimoto, S.; Ikuhara, Y. *Nano Lett.* **2012**, *12*, 6192−6197.
(34) Findlay, S. D.; Shibata, N.; Sawada, H.; Okunishi, E.; Kondo, Y.; Yamanoto, T.; Ikuhara, Y. *Appl. Phys. Lett.* **2009**, *95*, 191913.
(35) Findlay, S. D.; Shibata, N.; Sawada, H.; Okunishi, E.; Kondo, Y.; Ikuhara, Y. *Ultramicroscopy* **2010**, *110*, 903−923.
(36) Lim, J.; Moon, J.; Gim, J.; Kim, S.; Kim, K.; Song, J.; Kang, J.; Im, W. B.; Kim, J. *J. Mater. Chem.* **2012**, *22*, 11772−11777.
(37) Aritani, H.; Tanaka, T.; Funabiki, T.; Yoshida, S.; Kudo, M.; Hasegawa, S. *J. Phys. Chem.* **1996**, *100*, 5440−5446.
(38) Kuzmin, A.; Purans, J. *J. Phys.: Condens. Matter* **2000**, *12*, 1959−1970.
(39) Li, L. W.; Morrill, M. R.; Shou, H.; Barton, D. G.; Ferrari, D.; Davis, R. J.; Agrawal, P. K.; Jones, C. W.; Sholl, D. S. *J. Phys. Chem. C* **2013**, *117*, 2769−2773.
(40) Kang, J.-H.; Paek, S.-M.; Choy, J.-H. *Bull. Korean Chem. Soc.* **2010**, *31*, 3675−3678.
(41) Sathiya, M.; Rousse, G.; Ramesha, K.; Laisa, C. P.; Vezin, H.; Sougrati, M. T.; Doublet, M.-L.; Foix, D.; Gonbeau, D.; Walker, W.; Prakash, A. S.; Ben Hassine, M.; Dupont, L.; Tarascon, J.-M. *Nat. Mater.* **2013**, *12*, 827−835.
(42) Noh, H.-J.; Kim, B. J.; Oh, S.-J.; Park, J.-H.; Lin, H.-J.; Chen, C. T.; Lee, Y. S.; Yamaura, K.; Takayama-Muromachi, E. *J. Phys.: Condens. Matter* **2008**, *20*, 485208−485212.
(43) Scanlon, D. O.; Watson, G. W.; Payne, D. J.; Atkinson, G. R.; Egdel, R. G.; Law, D. S. L. *J. Phys. Chem. C* **2010**, *114*, 4636−4645.
(44) Lu, Y.-C.; Kwabi, D. G.; Yao, K. P. C.; Harding, J. R.; Zhou, J. G.; Zuin, L.; Shao-Horn, Y. *Energy Environ. Sci.* **2011**, *4*, 2999−3007.